Materials Chemistry and Physics 136 (2012) 347–357

Contents lists available at SciVerse ScienceDirect

Materials Chemistry and Physics

journal homepage: www.elsevier.com/locate/matchemphys

Investigation of local structure effect and X-ray absorption characteristics (EXAFS) of Fe (Ti) K-edge on photocatalyst properties of $SrTi_{(1-x)}Fe_xO_{(3-\delta)}$

M. Ghaffari [a,d,e,*], T. Liu [b], H. Huang [c], O.K. Tan [d], M. Shannon [e]

[a] Department of Electrical and Electronics Engineering, UNAM-Institute of Materials Science and Nanotechnology, Bilkent University, Ankara 06800, Turkey
[b] Institute for Synchrotron Radiation, Karlsruhe Institute of Technology, Hermann-von-Helmholtz-Platz 1, Eggenstein-Leopoldshafen 76344, Germany
[c] Surface Technology, Singapore Institute of Manufacturing Technology, 71 Nanyang Drive, Singapore 638075, Singapore
[d] School of Electrical and Electronic Engineering, Nanyang Technological University, 50 Nanyang Avenue, Singapore 639798, Singapore
[e] Mechanical Science and Engineering, University of Illinois at Urbana Champaign, Urbana, IL 61801, USA

HIGHLIGHTS

- STF_x catalyst prepared by a high temperature solid state reaction process.
- The electronic properties and local structure have been probed by EXAFS spectroscopy.
- The substitution of iron increases iron valence state and the Jahn–Teller ion formed.
- The Fe^{4+} ion causes disorder in the first shell and increases the oxygen vacancy defect.
- Iron doping led to decreasing of $[Ti(Fe)–O]_{ave}$ and increasing the photocatalyst property.

GRAPHICAL ABSTRACT

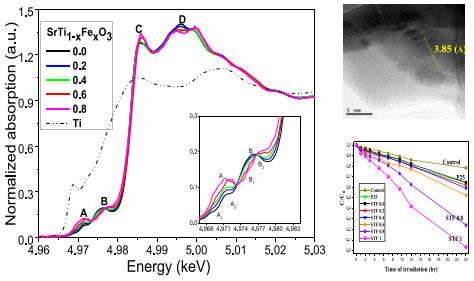

ARTICLE INFO

Article history:
Received 24 February 2012
Received in revised form
10 May 2012
Accepted 18 June 2012

Keywords:
$SrTi_{(1-x)}Fe_xO_{(3-\delta)}$
XAFS
Catalyst
Oxygen vacancies

ABSTRACT

In this study, the STF_x photocatalyst powder was synthesized with a high temperature solid state reaction. The microstructures and surface of samples were characterized by X-ray diffraction (XRD), scanning electron microscopy (SEM), transmission electron microscopy (TEM) and X-ray photoelectron spectroscopy (XPS). The electronic properties and local structure of the perovskite STF_x ($0 \leq x \leq 1$) systems were probed by extended X-ray absorption fine structure (EXAFS) spectroscopy. The XPS results revealed that with increasing iron doping, the amount of Fe^{3+} and Fe^{4+} increased significantly. The X-ray absorption data are discussed in detail with respect to the Fe (Ti) K-edge. The substitution of iron by titanium increased the Ti (Fe)–O first shell disorder factors that can be explained by increasing the oxygen vacancies. Oxygen vacancies or defects act as electron traps, which could capture the photo induced electrons and thus could effectively inhibit the recombination of the photo induced electrons and holes. Moreover due to the substitution of Ti with Fe, lattice shrinkage was observed and the largest derivation from the Gaussian distribution in STF_x was from those samples with $x = 0.6$ and $x = 0.8$. The substitution of iron by titanium increased the iron valence state, hence the formation of the Jahn–Teller Fe^{4+} ion. With increasing iron dopant the $[Ti(Fe)–O]_{ave}$ decreased and bond length of [Ti–O] and the consequent [Ti–O–Ti] increased and this phenomenon affected the photocatalyst and photo degradation properties of material and also decreased its efficiency.

* Corresponding author. Department of Electrical and Electronics Engineering, UNAM-Institute of Materials Science and Nanotechnology, Bilkent University, Ankara 06800, Turkey. Tel.: +65 6790 6537.
E-mail addresses: moha0094@e.ntu.edu.sg, mgh@illinois.edu (M. Ghaffari).

0254-0584/$ – see front matter © 2012 Elsevier B.V. All rights reserved.
http://dx.doi.org/10.1016/j.matchemphys.2012.06.037

1. Introduction

Since 1972, titanium dioxide (TiO_2) has been extensively studied as a photocatalyst due to its strong photo oxidizing potential, high stability, non-toxicity, and low cost [1]. However, the absorption pattern of pure TiO_2 needs to be extended to the visible light region for more efficient use of solar energy or under indoor light. To address this requirement many studies were initially focused on doping TiO_2 with transition metals [2–4]. However, the quantum yield of doped TiO_2 under visible-light irradiation is far lower than that of pristine TiO_2 under UV irradiation. Perovskite-type oxides of ABO_3 have attracted much attention as photocatalyst [5–8]. For example, strontium titanate, $SrTiO_3$, belongs to the perovskite family with a cubic structure and has the general formula of ABO_3. It is in the space group *Pm*3*m*, the coordination number of cation A is 12-fold and that for the B cation is 6-fold coordinated with the oxygen anions. Similar to TiO_2, the $SrTiO_3$ photocatalyst has also doped to shift its absorption toward the visible light range [7,9–19].

Recently, perovskite strontium titanate ferrite, $SrTi_{(1-x)}Fe_xO_{(3-\delta)}$ (STF in short), was found to possess redox behavior [18], gas sensing [12,14,20], fuel cell properties [12,20,21], oxygen separation membranes [22] and phase shifters in communication systems [23]. In terms of the bandgap energy of the $SrTi_{(1-x)}Fe_xO_{(3-\delta)}$, with increasing iron concentration of x from 0 to 1, the bandgap moves from 3.17 eV for $SrTiO_3$ to 1.80 eV for $SrFeO_3$ [10,16,20,24], which increases the visible light absorption of the STF. In addition, the defects and vacancies generated by the substitution of iron by titanium also benefit for the electron–hole pair separation of the STF photocatalyst [25–29]. Therefore, the microstructures and electronic properties of the STF are important for the photocatalytic properties, but unfortunately no systematic studies have been reported.

In this work, a series of $SrTi_{(1-x)}Fe_xO_{(3-\delta)}$ powders with different Fe doping were synthesized by solid state reaction method [30,31]. The electronic properties and local structure of the STF were studied with respect to their photocatalytic properties. In this paper we chose to study $SrTi_{(1-x)}Fe_xO_{(3-\delta)}$ composition, a potential photocatalyst, for their local structure and electronic properties. Our previous observation showed with increasing the iron content the photocatalyst properties of STF sample improved and STF_1 ($SrFeO_3$) showed the best results [30]. The local environment around Fe (Ti) centers, the local distortion and the first shell disorder factors throughout the whole x series, revealed by the X-ray absorption spectroscopy, were explained in connection with the observed catalytic properties. In addition, the morphology and crystal chemistry were characterized using the high resolution transmission electron microscopy (HRTEM) and the phase diagram and lattice parameters were investigated by quantitative X-ray diffraction (XRD). The catalytic kinetics and mechanism are addressed in more details in a separate paper [30]. Previous results showed with increasing the iron dopant the photocatalyst properties improved. In this paper, we discuss the role of local structure and oxygen vacancy in photocatalyst properties.

2. Experimental

2.1. Synthesis of the STF powders

The $SrTi_{(1-x)}Fe_xO_{(3-\delta)}$ powders were synthesized by solid state reaction. Strontium carbonates ($SrCO_3$), iron oxide (Fe_2O_3) and titanium oxide (anatase) were used as source materials and were purchased from Aldrich (99.9% pure). The strontium carbonate, iron oxide and titanium oxide powders were mixed and ground in an agate mortar, and the mixture was calcinated at 1200 °C for 24 h. Then, the calcined powders were ground again in the agate mortar, and were further calcined again at 1200 °C for another 24 h.

2.2. Microstructure characterizations

The phase structures of the STF powders were identified using a Shimadzu XRD-6000 X-ray diffractometer. The XRD patterns were collected over the angular range of 10–110° 2θ, with a scanning rate of 0.02° min^{-1}, using Bragg-Brentano geometry (Cu Kα source, primary and secondary Soller slits, 0.1 mm divergence slits, 0.3 mm receiving slit, and secondary graphite monochromator). The diffractometer was calibrated using a laboratory standard (NIST SRM 660a). The surface morphology of the samples was observed with a scanning electron microscopy (SEM; JEOL 6335F). The microstructures of the STF powders were observed by a Jeol JEM-2100F Transmission Electron Microscope (TEM) operated at 200 kV with 25 and 30 cm camera length. The selected area electron diffraction (SAED) patterns were also recorded to study the crystalline structures. The surface chemical composition of the powders were monitored by X-ray Photoelectron Spectroscopy (XPS) measurements performed with a Kratos Axis ULTRA X-ray Photoelectron Spectrometer and an Mg Kα anode (1253.6 eV photon energy, 15 kV, 300 W) at a take-off angle of 45°.

2.3. Extended X-ray absorption fine structure (EXAFS)

X-ray absorption spectroscopy is a useful tool to investigate the local structural and electronic properties of these compounds. The coordination chemistry of iron (titanium) is of particular interest. Information about the valence state and charge transfer of iron (titanium) can be obtained from the chemical shift of the absorption spectra, while the pre-edge features of the X-ray absorption near edge structure (XANES) region are related to the d-electron configuration and local symmetry of iron (titanium). The extended X-ray absorption fine structure (EXAFS) region can be used to probe local geometric structures up to several coordination shells around iron (titanium) ions, where the Fe–O (Ti–O) distance is of interest in connection with the valence state of iron. In this work, the Fe(Ti) K-edge X-ray absorption fine structure spectra were recorded at room temperature to investigate the local structures of Fe replaced $SrTi_{(1-x)}Fe_xO_{(3-\delta)}$ ($0 \le x \le 1$).

EXAFS experiments were carried out at room temperature at the X-ray Demonstration and Development (XDD) beamline of Singapore Synchrotron Light Source. The beamline provides a focused monochromatic X-ray source of 2.5–10 keV with a Si ⟨111⟩ monochromator. The experiments were carried out in transmission mode using two ion chambers which record the incident and transmitted X-ray intensities simultaneously. Each sample was ground into fine powders of 400 meshes, pressed into a pellet of 10 mm in diameter. The absorption spectra were recorded at room temperature as a function of photon energy at Ti and Fe K-edges. The data analysis was carried out using the WinXAS package [32]. Energies were calibrated using a Fe (Ti) foil standard, assigning the first inflection point to 7112 (4966) eV for Fe (Ti)-edge absorption data. A smooth pre-edge background was removed from each averaged spectrum by fitting a first-order polynomial to the pre-edge region, a second-order polynomial to the post-edge region and subtracting this polynomial from the entire spectrum; all data was normalized. A spline function was fitted to extract the EXAFS amplitude. The oscillations $\chi(k)$ were then obtained as a function of the photoelectron wave vector k and further, Fourier transforms weighted by k^3 over the range 3.1–13.1 $Å^{-1}$ for Ti and 2.8–12.6 $Å^{-1}$ for Fe. The first three shells of Fourier-transformed spectra were filtered out and fitted in the real space by the least square curve based on the single scattering theory [33]. The phase shift and backscattering amplitudes were extracted from the crystallographic data of $SrTiO_3$ and $SrFeO_3$, respectively. The inelastic factors, s_0^2 were

fixed to 0.95 and 0.72, respectively for Ti and Fe edge data, which were obtained by fitting to the standard references.

2.4. Photocatalytic properties

Photo degradation of methylene blue in water by STF_x powders was investigated. In addition, the anatase TiO_2 and Degussa P25 nanopowders were used for comparison. The samples were suspended in 10.8 μmol L^{-1} methylene blue (MB) aqueous solution by continuous magnetic stirring. The photocatalytic reaction was conducted in a 50-mL cell culture vessel illuminated by four 12-inch, 8-W fluorescent tubes (UVP Inc.) with UV filter. At given intervals of 1, 2, 3, 5, 7, 10, 12 and 24 h, the UV–visible spectra of all samples from 400 nm to 800 nm were recorded, and the remaining concentration of MB was analyzed by Shimadzu 2450 spectrophotometer. To investigate the kinetics of MB, a JIS R 1703-2 2007 standard was used and absorbance value of MB was taken by fixing the wavelength at 664 nm. The remaining MB in suspension was collected and one control sample without any catalyst was used to compare the results.

3. Results and discussions

3.1. Microstructures

The XRD patterns of the STF_x samples are shown in Fig. 1. All the diffraction peaks can be indexed by standard card number of 91062-ICSD, indicating the continuous solid solution of Fe in $SrTiO_3$. The XRD peaks shift to higher diffraction angle with increasing Fe concentrations, which is evidence for the increasing substitutional doping of Fe in STF_x. The ionic radius of Fe^{3+} (0.585 Å) is smaller than Ti^{4+} (0.605 Å), hence doping of Fe leads to a decreased lattice parameters and interplanar spacing in STF.

The Rietveld refinements of the XRD data were carried out using perovskite structure (space group: $PM\bar{3}M$) and 91062-ICSD standard card number to measure the crystallite size, lattice parameter, strain and oxygen vacancy. Rietveld analysis is a semi-quantitative method of analyzing the whole diffraction patterns of X-ray or neutron powder diffraction. In the Rietveld method, a single-number integrated intensity of I_{obs} is replaced (i.e. spread out) by a peak with heights y_i along the points of a step scan in 2-theta. The *R*-Bragg values for the different phases by Rietveld refinement are below 10, which are considered as authentic values for existence of above mentioned phases. The *R* values are useful indicators for the evaluation of a refinement, especially in the case of small improvements to the model, but they should not be over interpreted [20,34]. Fig. 2 shows the Rietveld pattern determined from X-ray powder diffraction data of $SrFeO_3$ powders. The vertical lines indicate possible Bragg peaks of the monoclinic $SrFeO_3$ phase.

The calculated values of crystallite size, lattice parameter, oxygen vacancy, lattice strain and *R*-Bragg of the STF_x samples are listed in Table 1. Doping of Fe increases the crystallites' size due to a high oxidization tendency. Moreover, the lattice parameters due to smaller ionic radius of the Fe compared to that for Ti, decrease from 3.9083 Å to 3.8601 Å. The oxygen vacancy per unit cell is a result of charge neutrality and hence the doping of Fe leads to higher structural disordering factors (σ^2). Local lattice strain shows a non-monotonous variation that can be explained by the lattice distortion and mismatch due to the radius difference. From the XRD analysis, the following Fe–O distances were obtained: 1.9524, 1.9470, 1.9420, 1.9373 and 1.9300 Å for the STF_x samples ($x = 0.2$, 0.4, 0.6, 0.8 and 1), respectively.

As shown by SEM micrographs in Fig. 3a and b, the $SrFeO_3$ powders calcined at 1200 °C have large particle size in the micro

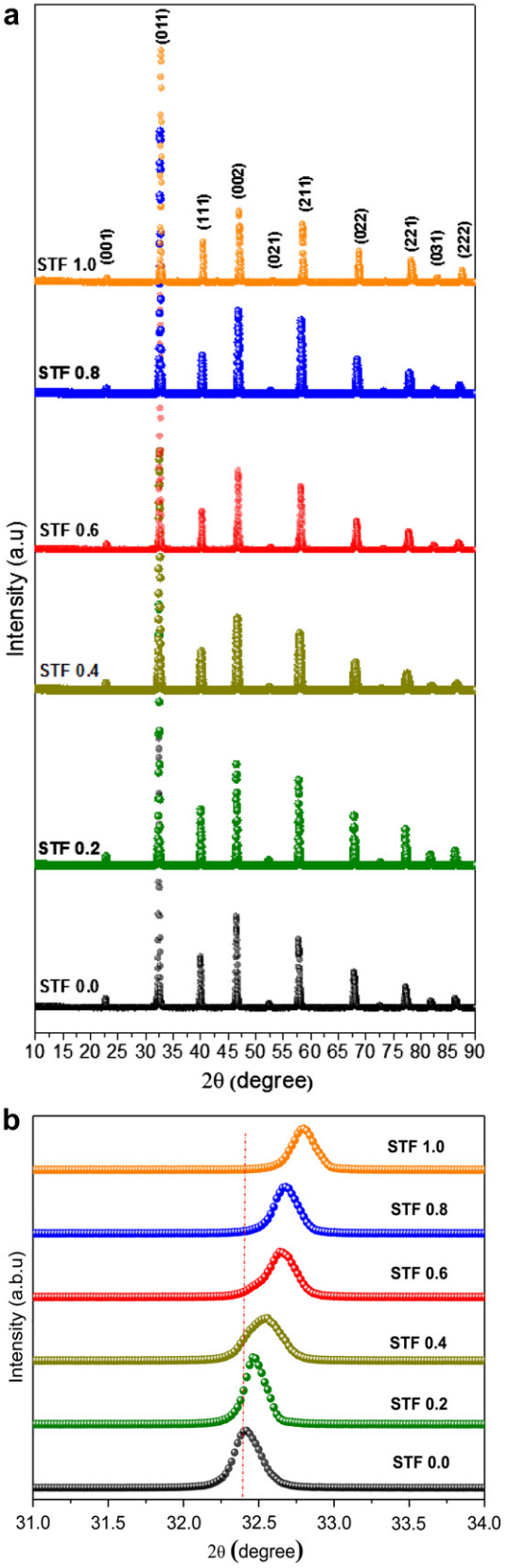

Fig. 1. (a) XRD patterns of the STF_x samples at different *x*; (b) a zoomed plot of the (011) diffraction peaks.

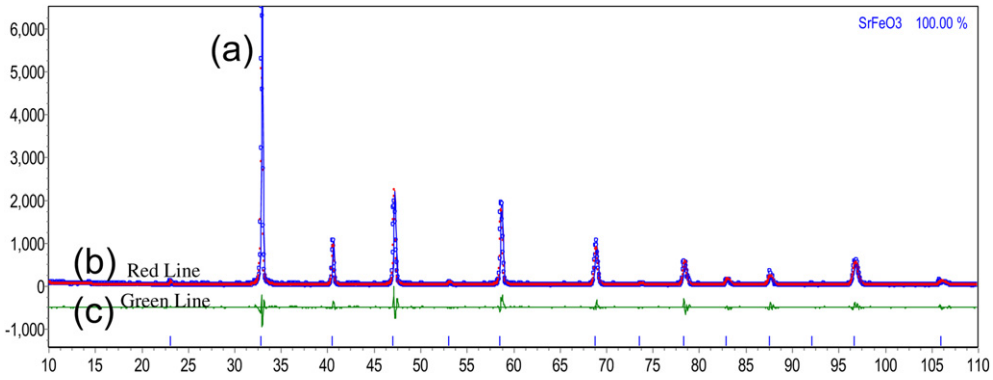

Fig. 2. Rietveld pattern determined from X-ray powder diffraction data for $SrFeO_3$. (Plots denote observed data (2a), the red line denotes calculated profiles (2b), and the green line denotes the difference (2c)). (For interpretation of the references to color in this figure legend, the reader is referred to the web version of this article.)

scale. The growth of particles is due to its high tendency to release the stress and defects such as dislocation and point defects at high temperature and increasing the rate of grain growth of particles by increasing the temperature to achieve sufficient activation energy. Fig. 3c and d shows the TEM images of the $SrFeO_3$ powders and corresponding selected area electron diffraction (SAED) pattern. The HRTEM image confirms the XRD results (Fig. 1). The lattice fringe spacing in the HRTEM is 3.86 Å which corresponds to the interspacing of (111) planes of pervoskite structure of $SrFeO_3$. The SAED patterns were (Fig. 3d) indexed using jems software. The SAED confirmed that strontium ferrite is well crystallized and the indexing of $SrFeO_3$ powder with [111].

3.2. XPS analysis

The surface compositions of the STF_x samples were studied by XPS. To illustrate the spectral features of the STF_x series samples, the O 1s and Fe2p peaks are summarized in Fig. 4a and b, respectively. Deconvolution of the O 1s spectra yields three peaks, namely O 1s a (529.0 eV), O 1s b (531.2 eV) and O 1s c (532.9 eV). From the literature, the peak at the 532.9 eV is probably due to the water and hydroxide absorbed on the surface [8,35–37], while the peaks at 531.2 eV corresponding to carbonates compounds and chemical adsorption [38–47]. The main peaks at 529.0 eV (O 1s a) correspond to the oxygen lattice [22,23,46,48]. Quantitative analysis has shown that with increasing iron content in STF_x powder, the amount of the oxygen lattice decreases. This observation can be attributed to the partial substitution of Fe with Ti, iron participation with mixed oxidation state of Fe^{3+} to Fe^{4+} and the formation of oxygen vacancy that consequently led to the reduction of the amount of oxygen lattice. The ratio of O 1s a presented in Table 2 shows that with increasing iron content this ratio decreased that can be explained by the formation of the oxygen vacancy with the Fe in Ti site.

The Fe 2p XPS region (Fig. 4b) shows a doublet of 2p3/2 and 2p1/; deconvolution of the Fe 2p spectra gives two components. Gaussian fitting of the peaks to the components of Fe^{3+} and Fe^{4+} is shown in Fig. 4b. The peaks at 710.1 eV (Fe 2p (a)) and 723.9 eV are similar to those reported for Fe 2p studies and the shake-up contribution at about 718.2 eV is consistent with the presence of Fe(III) [49–52]. The fitted results and the ratio of Fe^{3+} and Fe^{4+} are presented in Table 2. It was obvious that iron in STF_x perovskite structure is present as a mixture of Fe^{3+} and Fe^{4+} ($SrTi_{(1-x)}[Fe^{3+}, Fe^{4+}]_{(x)}O_{(3-\delta)}$) and with increasing iron dopant the amount of Fe^{3+} and Fe^{4+} increased significantly. Bocquet et al. investigated the electronic structure of the Fe^{4+} perovskite oxide $SrFeO_3$ by XPS, and concluded that the large increase in charge at the Fe site led to a chemical shift to a higher binding energy [49,50,52]. The doublet peaks that appear at 711.8 eV (Fe 2p (b)) and 725.6 eV could be assigned to Fe^{4+}. Moreover with increasing amount of Fe^{4+}, the shape of satellite peak also changed. P. Mills et al. [50,52] and other researchers [50,52] presented that the position of the satellite state is the key and fingerprint to detect the oxidation state of Fe. With changing oxidation state, the surface oxidation may also be changed. For α-Fe_2O_3, the shake-up satellite peaks located at around 718.2 eV were approximately 8 eV higher than the Fe 2p3/2 peak, whereas the satellite peak for FeO was approximately 6 eV from Fe $2p_{3/2}$ peak. There were no satellite peaks observed for Fe_3O_4 [50,52].

Bocquet et al. [49] used a p–d charge-transfer cluster-model calculation to interpret the Fe 2p core levels. They showed that for the Fe 2p core-levels XPS spectra, the strong satellite features were observed for the d5 compounds with an apparently weaker satellite present for $SrFeO_3$. Similarly, the spectrum for $SrFeO_3$ was primarily composed of main peaks due to the screened $\underline{c}d^5\underline{L}$ states and satellite structure from mixed $\underline{c}d^4$ and $\underline{c}d^6\underline{L}^2$ states [49].

Table 1
Crystallite size, lattice parameter, oxygen vacancy, lattice strain and *R*-Bragg values of STF_x samples that were calculated with Rietveld refinement.

x in STF_x	Crystallite size (nm)	Lattice parameter (nm)	Oxygen lattice	Oxygen vacancy (δ)	Lattice strain (%)	*R*-Bragg
0	243.6	0.3908	2.979	0.0207	0.0116 (L)	2.021
0.2	280.4	0.3901	2.927	0.0735	0.3519 (L)	2.132
0.4	320.2	0.3894	2.845	0.1554	0.6372 (L)	1.544
0.6	350.5	0.3884	2.793	0.2067	0.4981 (L)	2.554
0.8	378.3	0.3874	2.757	0.2466	0.2377 (L)	1.860
1	445.8	0.3860	2.743	0.2566	0.3348 (L)	7.98

Strain L means Lorentzian (this described the symmetrical part of an X-ray diffraction peak).

3.3. EXAFS measurement

The coordination chemistry of iron (titanium) is of particular interest. Information about the pre-edge features of the X-ray absorption near edge structure (XANES) region was related to the d-electron configuration and local symmetry of iron (titanium). The extended X-ray absorption fine structure (EXAFS) region was used to probe local geometric structures up to several coordination shells around iron (titanium) ions, where the Fe–O (Ti–O) distance was of interest in connection with the valence state of iron. The Fe and Ti K-edge XANES spectra for the STF_x samples at various x (0, 0.2, 0.4, 0.6, 0.8 and 1) are

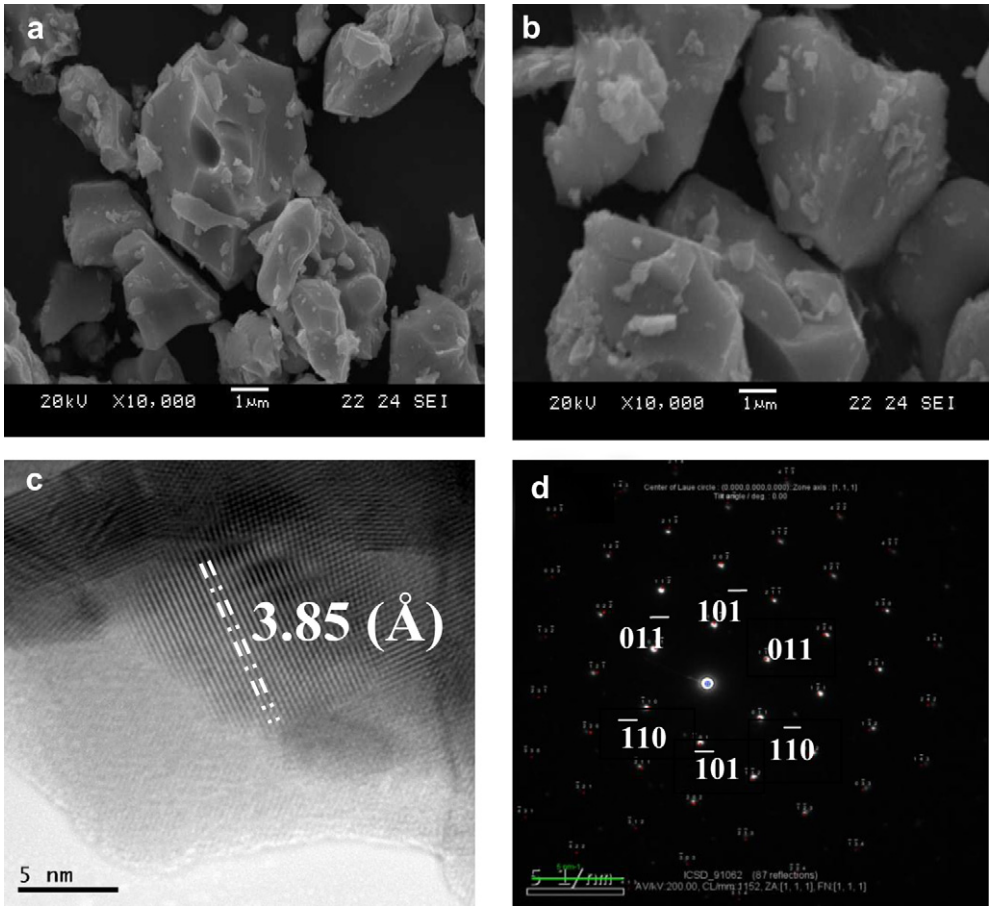

Fig. 3. SEM micrograph (×10,000) of the $SrFeO_3$ sample at two cycles of treatment (a) 1200 °C, Cycle 1, (b) 1200 °C, Cycle 2; (c) HRTEM micrograph of $SrFeO_3$ particles, (d) SAED patterns are indexed as $SrFeO_3$ with [111] zone axis.

shown in Fig. 5a and b, the standard Fe and Ti foils are also shown. Fig. 6 shows a schematic representation of the atomic orbitals for Fe^{+3} and Fe^{+4} and the expected K-edge XAS transitions to half occupied or empty orbitals and into the continuum. In an octahedral crystal field, the t_{2g} orbitals occur at lower energy than the e_g orbitals. This is a reflection of the orientation of the orbitals since the t_{2g} is directed between bond axes while the e_g points along bond axes. The Jahn–Teller Theorem predicts that distortions should occur for any degenerate state, including degeneracy of the t_{2g} level, however distortions in bond lengths are much more distinctive when the degenerate electrons are in the e_g level [49,53,54].

At the K-edge X-ray excitation, electrons of 1s orbitals are transferred to partially occupied or empty states (XANES region) nearby the Fermi level (3d and 4p-related orbitals), at higher energy X-rays electrons jump to the continuum (EXAFS region, where the outgoing electrons are scattered by neighboring atoms) [55–57]. Structural data on cubic perovskite ABO_3 (A = Sr, B = Ti, Fe) suggest that 6 oxygen atoms are observed in the cation first coordination sphere in position B [58]. The second and third coordination spheres contain 8 strontium atoms and 6 metal atoms, respectively [59]. The pre-edge peaks A and B, main peaks C and D can be seen in Fig. 5a.

The pre-edge peaks were related to a pure quadrupole origin due to 1s → 3d transitions in transitional metal oxides [60–62]. Under careful observation, the peak A for $SrTiO_3$ appears to be actually made of two peaks. As reported earlier [63,64], A_1 is a pure quadrupolar (E2), A_2 is partial quadrupolar (and partial dipolar), B is pure dipolar (E1). Even in $SrTiO_3$, a high distortion in TiO_6 was observed. The peak A for the perfect octahedral TiO_6 (Oh symmetry) located at lowest position and can be enhanced by a distortion to Oh due to the loss of centro-symmetry. It was suggested that the intensity of the peak B is proportional to a displacement of Ti atoms from the center of the TiO_6 octahedra [61] but inversely related to the Ti–O bond length. The peak C is a 4p-related "shape resonance" in the continuum part of the spectrum and the peak D is attributed to more delocalized states [65,66]. The XANES spectra show almost no edge shift as a function of x but their intensity and shape are changing systematically with x.

As shown in Fig. 5a, the intensity of pre-edge peak A increases with the increasing x of Fe content in the STF_x samples. Peak A is stronger than Peak B, and cannot be resolved into two peaks, while peak B shifts slightly to high energy. The peak C also slightly shifts toward high energy. Within the accuracy limit of XANES, any changes or splitting with the peak A in Fig. 5b cannot be detected. This may due to the more closely packed FeO_6 clusters and highly symmetry because of the smaller atomic radius for Fe. With increasing Fe dopant, the intensities of B_1 and B_2 and their ratios change continuously. No significant shift for the main peak was observed in Fig. 5b.

Fig. 7a and b shows the Ti K-edge and Fe K-edge EXAFS spectra of the STF samples after background removal. The radial structure functions $F(r)$ of STF samples obtained from Fourier transformation of their $k3\chi(k)$ are shown in Fig. 7a and b. After standard data reduction, the $\chi(k)$ k^3 function is shown in Fig. 7a and its Fourier

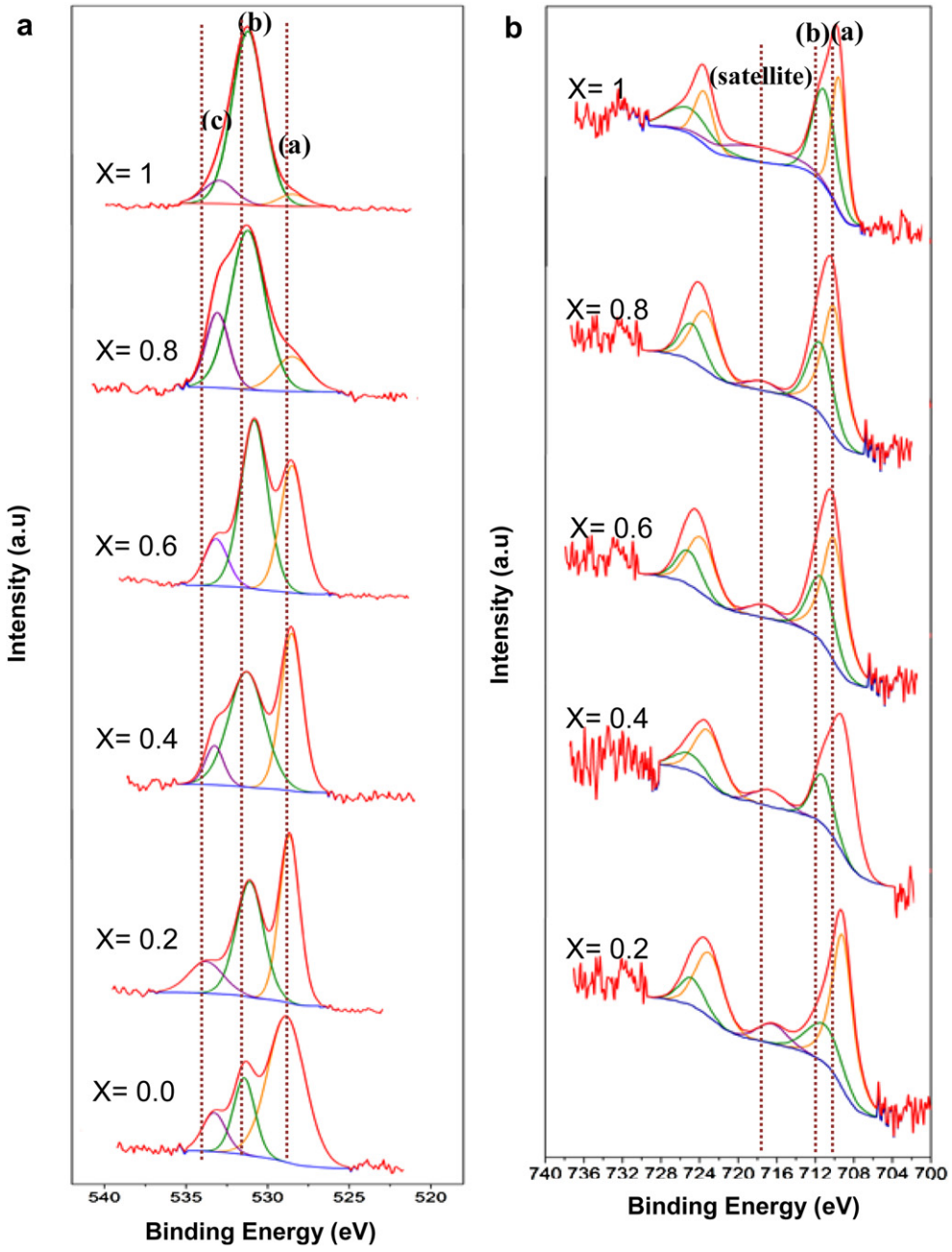

Fig. 4. The core level XPS spectra for STF for $x = 0–1$ for (a) O 1s, (b) Fe 2p.

transforms in Fig. 7b contain the information about the coordination geometry around each Ti. The first peak of the Fourier transform is due to the first Ti–O shell. The second peak contains the contribution from Ti–8Sr and Ti–6Ti(Fe) and the third shell is Ti–6Ti (Fe).

Table 2
Atomic concentrations calculated from XPS results for STF powders with $x = 0–1$.

	Atomic concentrations (%) for $SrTi_{(1-x)}Fe_{(x)}O_{(3-\delta)}$ @ different x					
	Ratio					
Elements	$x = 0$	$x = 0.2$	$x = 0.4$	$x = 0.6$	$x = 0.8$	$x = 1$
O 1s a	9.69	8.411	7.22	4.71	3.575	3.52
Fe^{+3}/Fe^{+4}	–	2.828	2.479	2.062	1.298	1.278

Two fitting models were applied which fit the first three shells, the coordination numbers (CN) were fixed, the first Ti–O shell was fitted by 4, 2 and 3, 3 respectively. The 4-2 model gave slightly better results and was presented as follows. In the two-coordination fitting to the first peak in the Fourier-transform, the Ti–O coordination shows the effect of the Ti displacement in TiO_6 directly. The second peak is due to the eight Sr neighbors at the distance of 3.38 Å, and the third peak is due to Ti or Fe atoms in adjacent unit cells at the distance of 3.90 Å, contributing mainly from the linear Ti–O–Ti paths.

Using the 4-2 fitting model, two kinds of Ti–O coordinations are identified, assuming a typical Ti–O (4) (intra-bilayer, bond length R_1) and Ti–O(2) (inter-bilayer, bond length R_2), the Coordination number (CN) is set to 4 and 2, respectively. The fitted R_1, R_2, and the mean-square relative displacement or the Debye–Waller

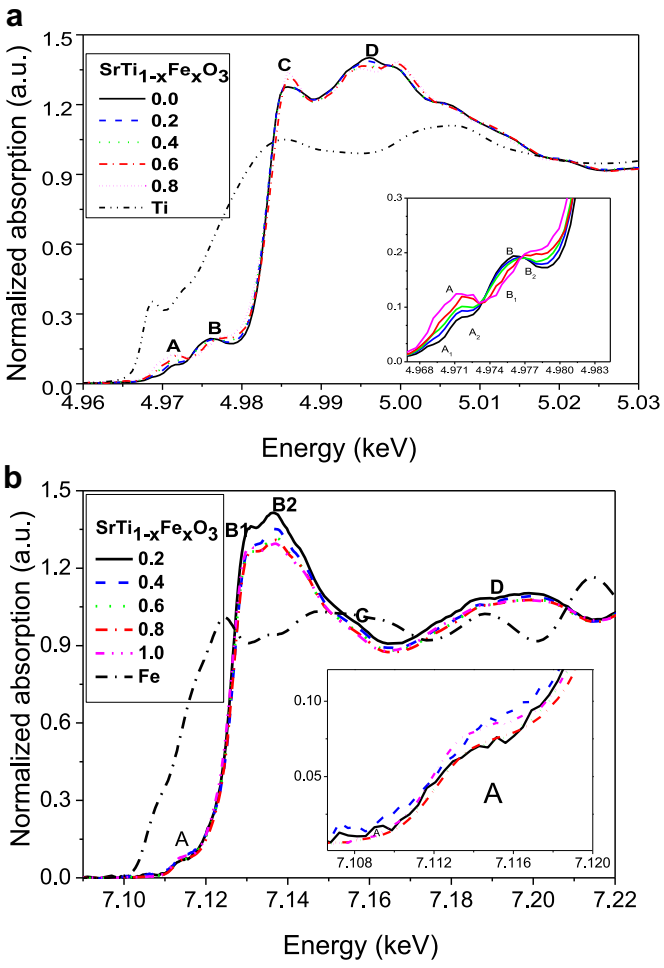

Fig. 5. Ti K-edge (a) and Fe K-edge (b) XANES spectra of the $SrFe_xTi_{(1-x)}O_3$ samples at $x = 0$, 0.2, 0.4, 0.6, 0.8, 1. The inset in (a) is pre-edge peaks for Ti K-edge and (b) Fe K-edge.

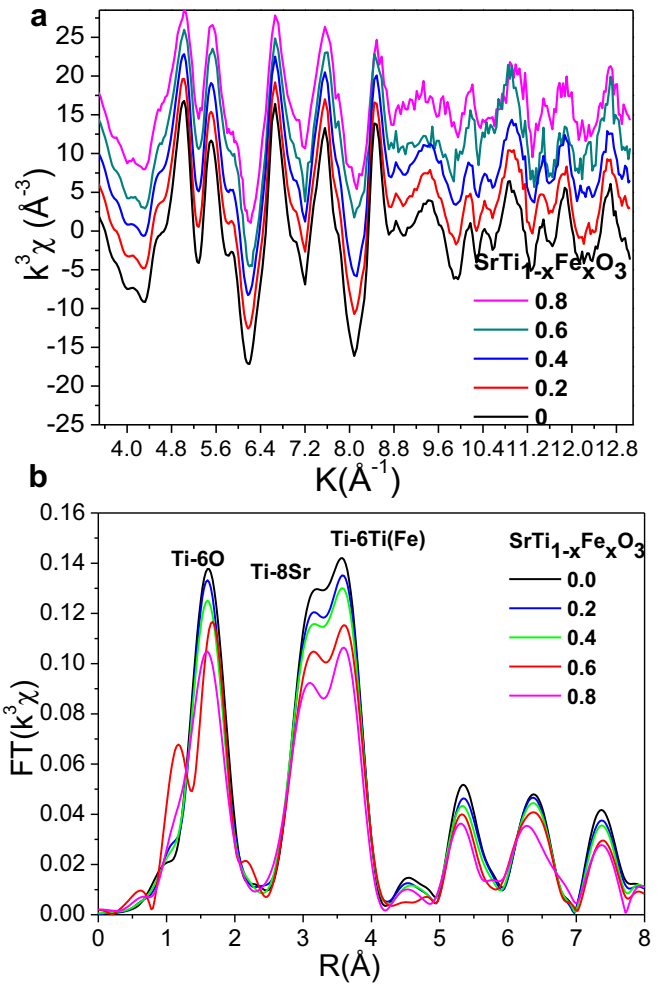

Fig. 7. (a) Ti K-edge EXAFS functions, $\chi(k)\,k^3$ of the $SrFe_xTi_{(1-x)}O_3$ samples (x: 0, 0.2, 0.4, 0.6, 0.8, 1.0); (b) Fourier transforms of the EXAFS signals in (a), phase shifts were not corrected.

factors σ_1^2 and σ_2^2 are reported in Table 3 as a function of x. The bond length of Ti–O(2) R_2 is much shorter for the $x = 0.6$ and 0.8; these two samples indicate a large distortion in TiO_6. An attempt to fit the $x = 0$ sample with two Ti–O shell was not successful, meaning the TiO_6 in $SrTiO_3$ is relatively less distorted, and introducing Fe has induced a significant displacement of oxygen atoms in the inter-bilayer. Such local distortions may induce some additional energy band splitting near the Fermi level. In addition, the bond length change for the Ti–Ti (Fe) shell is not significant, the Ti–Ti and Ti–Fe are not distinguishable in this shell. Hence it may also contain some Ti–Fe component, but for simplicity, it was fit by only Ti–Ti shells. In the cubic phase of perovskites, the scattering intensity of the third peaks is much larger, this is from the "shadow effect" of the linear Ti–O–Ti(Fe) bond [64,67,68]. For Ti K-edge data in the STF_x samples when the Ti content of the samples increases, such as in $SrTi_{0.2}Fe_{0.8}O_3$ and $SrFeO_3$, their shoulder peaks shift to low-R direction at about 0.12 nm. Moreover, significant disorder in EXAFS leads to shells not being seen or having severely reduced amplitude compared to that expected and disorder effects affect the amplitude of the EXAFS [69]. As the Ti content decreases, the amplitude of the Radial distribution functions (RDF), shown in Fig. 7b, becomes weaker and weaker (top to bottom in Fig. 7b). Comparing their structural disordering factor (σ_2) presented in Table 3, it was observed that the disordering of Ti coordination in STF samples increased with the Fe content.

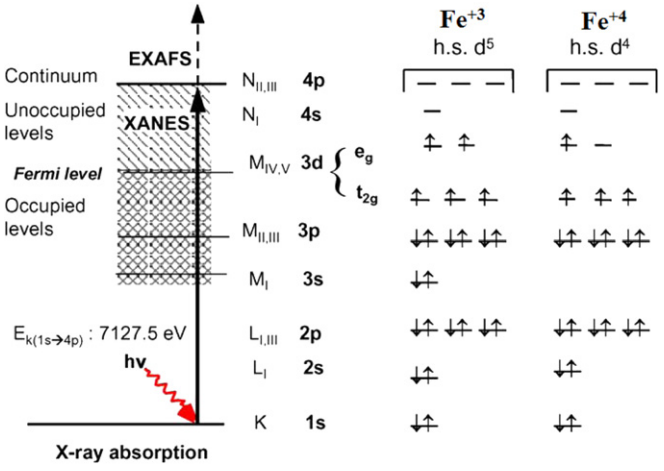

Fig. 6. Molecular orbital scheme of Fe^{+3} and Fe^{+4} with possible XAS transitions.

The increase of the Ti (Fe)–O first shell disorder factors can be explained by the increasing oxygen vacancy seen in the XRD results data. At the Fe K-edge absorption near edge, the 1s → 3d quadrupole transition and 1s → 4p dipole transition followed by ligand to metal charge transfer (LMCT) process are shifted to lower energy with increase of the x value, which represents the Fe–O bond

Table 3
Coordination number (CN), the bond length and Debye–Waller factors at the Ti K-edge EXAFS of the $SrFe_xTi_{(1-x)}O_3$ samples at $x = 0$, 0.2, 0.4, 0.6 and 0.8. The error bars are 10% for σ^2, 0.01 Å for Ti–O1 Ti–O2 and 0.02 Å for Ti–Sr and Ti–Ti.

$SrTi_{(1-x)}Fe_{(x)}O_3$	$x = 0$			$x = 0.2$			$x = 0.4$			$x = 0.6$			$x = 0.8$		
Bond lengths	CN	R (Å)	σ^2 (10^{-3} Å^{-2})	CN	R (Å)	σ^2 (10^{-3} Å^{-2})	CN	R (Å)	σ^2 (10^{-3} Å^{-2})	CN	R (Å)	σ^2 (10^{-3} Å^{-2})	CN	R (Å)	σ^2 (10^{-3} Å^{-3})
$[Ti–O]_1$	6	1.96	6.7	4	1.95	6.7	4	1.94	6.9	4	1.93	5	4	1.94	7.5
$[Ti–O]_2$	–	–	–	2	1.93	3	2	1.91	3	2	1.74	3	2	1.73	3
[Ti–Sr]	8	3.39	8.1	8	3.36	12.5	8	3.35	13.2	8	3.34	14	8	3.32	13.9
[Ti–Ti]	6	3.96	1.4	6	3.98	5.2	6	3.98	5.9	6	3.99	6.9	6	3.97	6.3

covalency decreasing systematically [70]. The pre-edge features (Fe 1s → 3d transitions) reveal an intensity increase with increasing x, suggesting an increase in the Fe valence state upon titanium substitution [56,71]. Fig. 8a and b presents the experimental Fe K-edge EXAFS signals of the $\chi(k)$ k^3 functions and its Fourier transform. XAFS analyses of the Fe K-edge EXAFS spectra also support the XRD and XANES results. The Fourier transform of the $\chi(k)$ k^3 (Fig. 7b) reveals a strong reduction of the Ti–O shell radius in accordance with the formation of Fe^{4+} proportional to x. Normally, this would be attributed to a decrease in coordination number. The main reason for this decrease in intensity in Figs. 7b and 8b are most probably due to the formation of the Jahn–Teller Fe^{4+} ion (h.s. d4), which leads to a distorted FeO_6 octahedron associated with an anomalous increase in the Debye–Waller factor [56,71]. Iron participated in $SrFeO_3$ structure with valence Fe^{4+} as well that observed previously by Bocquet et al. [49]. Due to the correlation observed for the EXAFS parameters s_0^2, σ^2 and CN, a more reliable fit was performed by fixing CN = 6 for Fe–O, CN = 8 for Fe–Sr and CN = 6 for Fe–Fe(Ti) bonds in most stoichiometries. The exception is the $x = 0.2$ sample, in which a two Fe–O shell must be adopted, this hints a maximum distortion for the $x = 0.2$. Table 4 lists the coordination number (CN), bond length and Debye–Waller factors for Fe K-edge data in the STF_x samples (x: 0, 0.2, 0.4, 0.6, 0.8, and 1.0). From these data there are no any noticeable changes for R_1(Fe–O), 1.91–1.93 Å, and σ^2 (Fe–O). It should be mentioned once again that the data for Fe–Fe should include both Fe–Fe and Fe–Ti (which is not distinguishable) coordinations.

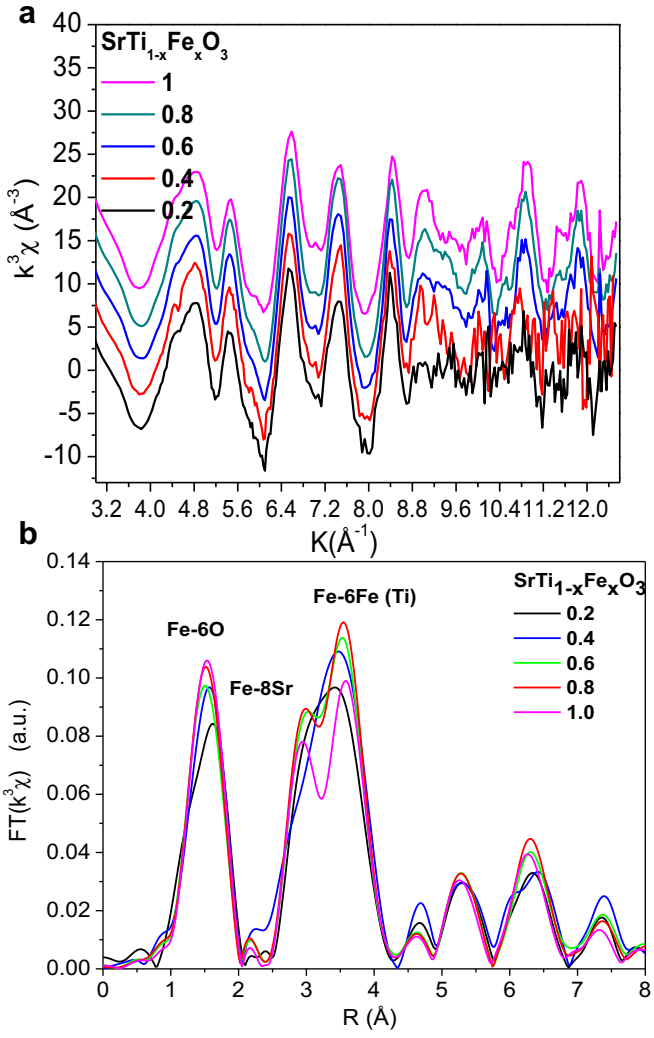

Fig. 8. (a) Experimental Fe K-edge EXAFS signals of the $\chi(k)$ k^3 functions and (b) Fourier transforms of the EXAFS functions for the $SrFe_xTi_{(1-x)}O_3$ samples (x: 0, 0.2, 0.4, 0.6, 0.8, 1.0), phase shift was not corrected.

There is a linear relation between the Fe–O bond length and the iron valence number [72]. In iron oxides (CN = 6), the Fe–O bond length reduces as Fe valence gets higher, such as in compounds FeO (2+, 2.10 Å), α-Fe_2O_3 (3+, 2.00 Å], $SrFeO_3$ [4+, 1.90 Å) [49,64,72]. The shorter Fe–O distance listed in Table 4 also implies some tetravalent Fe may exist, consistent with the analysis reported in Refs. [73,74]. Moreover valence of Ti is 4+ in TiO_6 and the Ti–O distance in STF is similar to other Ti 4+ oxides (TiO_2) thus with Fe replacement, Fe remains also a short Fe–O distance, meaning Fe is mostly 4+ (actually are mixing of the 3+ and +4). As presented in Tables 3 and 4, with increasing iron dopant the $[Ti(Fe)–O]_{ave}$ (measured by equation (1)) decreased and also there are some reports explaining that by increasing the bond length of [Ti–O] the consequent [Ti–O–Ti] increased that is due to the formation of titanium oxide crystal and this phenomenon affects the photocatalyst and photo degradation properties of material and its efficiency also decreased [75,76].

According to the obtained data (Figs. 7 and 8, Tables 3 and 4), the iron and titanium surrounding is highly symmetric and does not depend on the oxide stoichiometry [59]. Fig. 9(a) and (b) shows a plot of all interatomic distances from the fitting results of EXAFS data as a function of x. The distances determined by EXAFS analysis exhibit a more detailed picture with different Ti–O and Fe–O distances for the same sample. The plotted distance for Ti–O and Fe–O is the average of [Ti (Fe)–O] of 1 and 2 that is measured by;

$$\text{Average } R = (CN_1{*}R_1 + CN_2{*}R_2)/(CN_1 + CN_2) \quad (1)$$

In Fig. 9 for the STF_x samples, the Ti–O distance remains essentially constant, at about 1.95 Å the same as in $SrTiO_3$, while the Fe–O distances stay close to that in $SrFeO_3$ 1.91 Å for large x and increase only for $x > 0.4$. Note that the first shell of the TiO_6 and FeO_6 is compactly stacked that changes little with x. The second shell for Ti–Sr and Fe–Sr, R reduces significantly with increasing x. In addition, in the third shell of Ti–Ti(Fe) and Fe–Fe(Ti), using R to estimate lattice parameters, the theoretical values are 3.90 Å for $SrTiO_3$ and 3.85 Å for $SrFeO_3$. The uncertainties for these measurements were ±0.01 Å for R1 and ±0.02 Å for R2 and R3.

Clearly, the substitution of iron by titanium increased the oxygen vacancy. And as explained above oxygen vacancies/defects

Table 4
Coordination number (CN), the bond length and Debye–Waller factors at Fe K-edge EXAFS of the $SrFe_xTi_{(1-x)}O_3$ samples at $x = 0.2$, 0.4, 0.6, 0.8 and 1.0. The error bars are 10% for σ^2, 0.01 Å for Ti–O1 Ti–O2 and 0.02 Å for Ti–Sr and Ti–Ti.

$SrTi_{(1-x)}Fe_{(x)}O_3$	$x = 0.2$			$x = 0.4$			$x = 0.6$			$x = 0.8$			$x = 1$		
Bond lengths	CN	R (Å)	σ^2 (10^{-3} Å^{-2})	CN	R (Å)	σ^2 (10^{-3} Å^{-3})	CN	R (Å)	σ^2 (10^{-3} Å^{-3})	CN	R (Å)	σ^2 (10^{-3} Å^{-3})	CN	R (Å)	σ^2 (10^{-3} Å^{-3})
[Fe–O]	4	1.93	8	–	–	–	–	–	–	–	–	–	–	–	–
[Fe–O]	2	1.72	6.9	6	1.92	7.8	6	1.90	7.7	6	1.90	7	6	1.91	6.6
[Fe–Sr]	8	3.35	12	8	3.37	8.6	8	3.34	7.9	8	3.33	7.9	8	3.30	9.3
[Fe–Fe]	6	3.93	6.8	6	3.92	2	6	3.90	1.4	6	3.91	1.1	6	3.92	2.3

act as electron traps, which could capture the photo induced electrons and thus could effectively inhibit the recombination of the photo induced electrons and holes [27–29]. Furthermore, when these traps are close enough to the surface, the trapped electrons can react with oxygen. The iron doping generated more oxygen vacancies and/or defects, which could capture the photo induced electrons and thus could effectively inhibit the recombination of the photo induced electrons and holes. EXAFS study also confirmed that with increasing the substitution of iron by titanium, the structure disorder of STF samples also increase that is related to producing the defects and oxygen vacancy. These data show a good consistency with XRD, Rietveld analysis that presented in Table 1 and XPS analysis. Moreover, defects could be regarded as another factor that affects the catalytic activity of STF. The amount of oxygen vacancy can examine by XRD or increase of the first shell disorder factors. The structure disorder of the sample could be regarded as another factor that affects the catalytic activity of STF and the sample with greater σ^2 would provide more oxygen vacancies and/or defects and suitable surface sites.

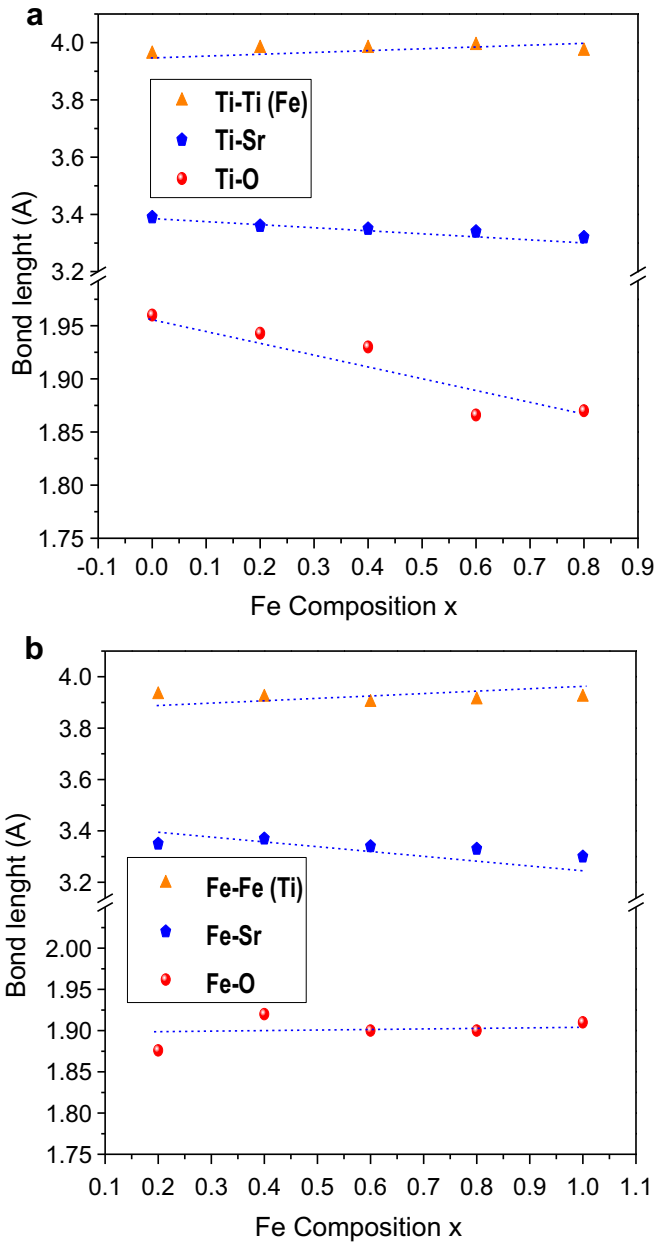

Fig. 9. Composition dependence of the bond length in $SrFe_xTi_{(1-x)}O_3$ samples (x: 0, 0.2, 0.4, 0.6, 0.8, 1.0) from the first three coordination shells. (a) Ti K-edge and (b) Fe K-edge.

3.4. Photocatalytic activity

Fig. 10 shows the MB degradation by STF_x powders with $x = 0$, 0.2, 0.4, 0.6, 0.8 and 1 under fluorescent light illumination from 0 to 24 h. With increasing Fe content from $x = 0$ to 1, the photocatalytic activity of the STF_x powders increases, which is consistent with previous results [10,77]. In comparison, P25 (TiO_2) nanopowders show fast degradation of MB only in the UV range. The control sample (MB dissolved in DI water without any catalyst) shows almost no photocatalytic activity. Among all samples, $SrFeO_3$ (STF_1) showed the best performance. This observation can explain by increasing the oxygen vacancy during iron doping. As explained before oxygen vacancies/or defects act as electron traps, which could capture the photo induced electrons and thus could effectively inhibit the recombination of the photo induced electrons and holes and increase the photocatalyst properties.

4. Conclusion

The results obtained by combined in situ UV–vis spectra, XRD, and XAFS spectroscopies are very important for a fundamental understanding of the chemical structures of the $SrFe_xTi_{(1-x)}O_3$ with different ratios of Ti/Fe. The XPS analysis showed that iron in STF_x perovskite structure participated in the mixture of Fe^{3+} and Fe^{4+} ($SrTi_{(1-x)}[Fe^{3+}, Fe^{4+}]_{(x)}O_{(3-\delta)}$). With increasing iron dopant, the amount of Fe^{3+} and Fe^{4+} increased significantly. Oxygen vacancy was formed. Consequently, with increasing oxygen vacancy, the amount of oxygen lattice would reduce. This observation can explain by bond length of [Ti–O] and [Ti–O–Ti]. With increasing iron dopant the $[Ti(Fe)–O]_{ave}$ decreased and bond length of [Ti–O] and the consequent [Ti–O–Ti] increased that is due to the formation of titanium oxide crystal and this phenomenon affects the photocatalyst and photo degradation properties of material and its efficiency also decreased.

The local electronic structure of $SrFe_xTi_{(1-x)}O_3$ ($0 \leq x \leq 1.0$) investigated by XANES showed a dependence on composition as well as on iron oxidation state. In the $SrFe_xTi_{(1-x)}O_3$ system, the peak at ~1.90 Å in the Fourier transformed EXAFS spectra is due to the first coordination shell, i.e., the nearest six oxygen atoms

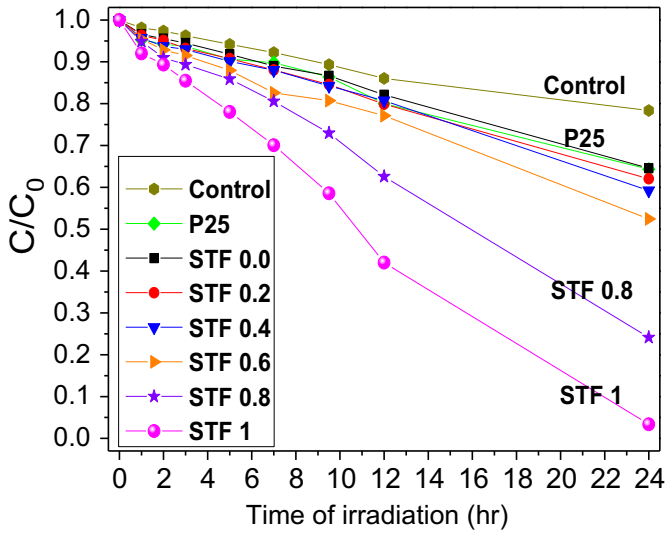

Fig. 10. Methylene blue degradation by high temperature STF_x powder with different composition.

surrounding Fe. The second peak at ~3.3 Å is due to the next nearest neighbors Sr, and the third peak at ~3.9 Å is assigned to the Fe–Fe contribution. EXAFS analysis indicates that all samples have quite similar local structure. The peaks A and B (Ti K-edge) reveal an intensity increase with increasing *x*, suggesting an increase in the Fe valence state upon iron substitution. The Fe K-edge XANES spectra (peak C) of $SrFe_xTi_{(1-x)}O_3$ are shifted to higher energies with increasing *x*, which is also an indication for an increase in the valence state of iron. The strong decrease of the intensity of the Fourier-transformed Chi $x\ k^3$ functions is probably due to an increase of the Debye–Waller factor arising from the production of Jahn–Teller distorted Fe(IV) O6 octahedrons, rather than a decrease of the oxygen coordination number. Results from these experiments indicate that Fe XANES can identify the presence of Fe(6) in a sample. It has been shown that, for the samples measured in this study, the Fe–O bond length is linearly related to the iron valence regardless of the Fe–O coordination number (consistent with valence-dependent ionic radii tables). From the XAFS spectra, the Fe–O, Fe–Sr and Fe–Fe bonding were observed around iron. The chemical state of iron was determined from the results of Fe–O bond lengths. The average Fe–O bond length in the layer is smaller than that for Fe_2O_3 and FeO. This increase in the Fe–O bond length is due to the increase in the Fe-valance state. The structure disorder of the sample could be regarded as another factor that affects the catalytic activity of STF and the sample with greater σ^2 would provide more oxygen vacancies and/or defects and suitable surface sites.

Acknowledgements

The authors would like to thank the faculty of Singapore Synchrotron Light Source (SSLS) in National University of Singapore for providing the experimental facilities. Moreover the authors would like to thank Dr. Agnieszka for her kind help in this work.

References

[1] A. Fujishima, K. Honda, Electrochemical photolysis of water at a semiconductor electrode, Nature 238 (1972) 37–38.
[2] F. Gracia, J.P. Holgado, A. Caballero, A.R. Gonzalez-Elipe, Structural, optical, and photoelectrochemical properties of Mn^+–TiO_2 model thin film photocatalysts, The Journal of Physical Chemistry B 108 (2004) 17466–17476.
[3] H. Haick, Y. Paz, Long-range effects of noble metals on the photocatalytic properties of titanium dioxide, The Journal of Physical Chemistry B 107 (2003) 2319–2326.
[4] E. Reddy, B. Sun, P. Smirniotis, Transition metal modified TiO_2-loaded MCM-41 catalysts for visible-and UV-light driven photodegradation of aqueous organic pollutants, Journal of Physical Chemistry B 108 (2004) 17198–17205.
[5] S. Ahuja, T. Kutty, Nanoparticles of $SrTiO_3$ prepared by gel to crystallite conversion and their photocatalytic activity in the mineralization of phenol, Journal of Photochemistry and Photobiology A: Chemistry 97 (1996) 99–107.
[6] T. Ishii, H. Kato, A. Kudo, H_2 evolution from an aqueous methanol solution on $SrTiO_3$ photocatalysts codoped with chromium and tantalum ions under visible light irradiation, Journal of Photochemistry and Photobiology A: Chemistry 163 (2004) 181–186.
[7] R. Konta, T. Ishii, H. Kato, A. Kudo, Photocatalytic activities of noble metal ion doped $SrTiO_3$ under visible light irradiation, Journal of Physical Chemistry B 108 (2004) 8992–8995.
[8] C. Wagner, D. Zatko, R. Raymond, Use of the oxygen KLL Auger lines in identification of surface chemical states by electron spectroscopy for chemical analysis, Analytical Chemistry 52 (1980) 1445–1451.
[9] E. Bakken, S. Stølen, T. Norby, R. Glenne, M. Budd, Redox energetics of $SrFeO_{3-[\delta]}$ – a coulometric titration study, Solid State Ionics 167 (2004) 367–377.
[10] N. Cheremisinoff, P. Cheremisinoff, R. Tratter, Chemical and Nonchemical Disinfection, Ann Arbor, 1981.
[11] V.L. Kozhevnikov, I.A. Leonidov, M.V. Patrakeev, E.B. Mitberg, K.R. Poeppelmeier, Electrical properties of the ferrite $SrFeO_y$ at high temperatures, Journal of Solid State Chemistry 158 (2001) 320–326.
[12] C. Liang, D. Yang, Z. Yang, F. Hou, M. Xu, The preparation and oxygen sensitivity of strontium ferrite thin films, Surface and Coatings Technology 200 (2005) 2515–2517.
[13] M. Miyauchi, M. Takashio, H. Tobimatsu, Photocatalytic activity of $SrTiO_3$ codoped with nitrogen and lanthanum under visible light illumination, Langmuir 20 (2003) 232–236.
[14] R. Moos, K. Hardtl, Defect chemistry of donor doped and undoped strontium titanate ceramics between 1000 °C and 1400 °C, Journal of the American Ceramic Society 80 (1997) 2549–2562.
[15] T. Ohno, T. Tsubota, Y. Nakamura, K. Sayama, Preparation of S, C cation-codoped $SrTiO_3$ and its photocatalytic activity under visible light, Applied Catalysis A: General 288 (2005) 74–79.
[16] A. Rothschild, W. Menesklou, H. Tuller, E. Ivers-Tiffée, Electronic structure, defect chemistry, and transport properties of $SrTi_{1-x}Fe_xO_{3-y}$ solid solutions, Chemistry of Materials 18 (2006) 3651–3659.
[17] D. Smith, E. Chang, D. Liu, Travels through perovskite space, Phase Transitions 58 (1996) 57–73.
[18] Y. Wang, J. Chen, X. Wu, Preparation and gas-sensing properties of perovskite-type $SrFeO_3$ oxide, Materials Letters 49 (2001) 361–364.
[19] W. Xiao, New Materials Systems for Advanced Tribological and Environmental Applications (2006).
[20] S. Steinsvik, R. Bugge, J.O.N. GjØNnes, J. TaftØ, T. Norby, The defect structufe of $SrTi_{1-x}Fe_xO_{3-y}$ (x = 0–0.8) investigated by electrical conductivity measurements and electron energy loss spectroscopy (EELS), Journal of Physics and Chemistry of Solids 58 (1997) 969–976.
[21] S.J. Skinner, J.A. Kilner, Oxygen ion conductors, Materials Today 6 (2003) 30–37.
[22] J.R. Jurado, F.M. Figueiredo, B. Gharbage, J.R. Frade, Electrochemical permeability of $Sr_{0.7}(Ti, Fe)O_{3-[\delta]}$ materials, Solid State Ionics 118 (1999) 89–97.
[23] V. Varadan, D. Ghodgaonkar, V. Varadan, J. Kelly, P. Glikerdas, Ceramic phase shifters for electronically steerable antenna systems, Microwave Journal 35 (1992) 116–127.
[24] A. Rothschild, S.J. Litzelman, H.L. Tuller, W. Menesklou, T. Schneider, E. Ivers-Tiffée, Temperature-independent resistive oxygen sensors based on $SrTi_{1-x}Fe_xO_{3-[\delta]}$ solid solutions, Sensors and Actuators B: Chemical 108 (2005) 223–230.
[25] L.H. Brixner, Preparation and properties of the system, Materials Research Bulletin 3 (1968) 299–308.
[26] K. Sahner, D. Schonauer, R. Moos, M. Matam, M. Post, Effect of electrodes and zeolite cover layer on hydrocarbon sensing with p-type perovskite $SrTi_{0.8}Fe_{0.2}O_{3-d}$ thick and thin films, Journal of Materials Science 41 (2010).
[27] H. Gerischer, A. Heller, The role of oxygen in photooxidation of organic molecules on semiconductor particles, The Journal of Physical Chemistry 95 (1991) 5261–5267.
[28] A.K. Ghosh, F.G. Wakim, R.R. Addiss, Photoelectronic processes in rutile, Physical Review 184 (1969) 979.
[29] W. Siripala, M. Tomkiewicz, Observation of "intrinsic" surface states at the TiO_2 aqueous-electrolyte interface by band-gap electroreflectance spectroscopy, Physical Review Letters 50 (1983) 443.
[30] M. Ghaffari, P.Y. Tan, M.E. Oruc, O.K. Tan, M.S. Tse, M. Shannon, Effect of ball milling on the characteristics of nano structure $SrFeO_3$ powder for photocatalytic degradation of methylene blue under visible light irradiation and its reaction kinetics, Catalysis Today 161 (2011) 70–77.
[31] M. Ghaffari, H. Huang, P. Tan, O. Tan, Synthesis and visible light photocatalytic properties of $SrTi_{(1-x)}Fe_xO_{3-\delta}$ powder for indoor decontamination, Powder Technology (2012).
[32] T. Ressler, WinXAS: a program for X-ray absorption spectroscopy data analysis under MS-windows, Journal of Synchrotron Radiation 5 (1998) 118–122.

[33] E. Stern, Theory of the extended X-ray-absorption fine structure, Physical Review B 10 (1974) 3027–3037.
[34] L.B. McCusker, R.B. Von Dreele, D.E. Cox, D. Louer, P. Scardi, Rietveld refinement guidelines, Journal of Applied Crystallography 32 (1999) 36–50.
[35] D. Briggs, M. Seah, Practical surface analysis by Auger and X-ray photoelectron spectroscopy, in: D. Briggs, M.P. Seah (Eds.), John Wiley & Sons, Chichester, 1983. xiv±533.
[36] B. Löchel, H. Strehblow, M. Sakashita, Breakdown of passivity of nickel by fluoride, Journal of the Electrochemical Society 131 (1984) 522.
[37] Q. Wu, M. Liu, W. Jaegermann, X-ray photoelectron spectroscopy of $La_{0.5}Sr_{0.5}MnO_3$, Materials Letters 59 (2005) 1480–1483.
[38] N. Batis, P. Delichere, H. Batis, Physicochemical and catalytic properties in methane combustion of $La_{1-x}Ca_xMnO_{3-y}$ ($0 \ll x \ll 1$; $-0.04 \ll y \ll 0.24$) perovskite-type oxide, Applied Catalysis A: General 282 (2005) 173–180.
[39] D. Fino, N. Russo, E. Cauda, G. Saracco, V. Specchia, La–Li–Cr perovskite catalysts for diesel particulate combustion, Catalysis Today 114 (2006) 31–39.
[40] S.M. Lima, J.M. Assaf, M.A. Peña, J.L.G. Fierro, Structural features of $La_{1-x}Ce_xNiO_3$ mixed oxides and performance for the dry reforming of methane, Applied Catalysis A: General 311 (2006) 94–104.
[41] B. Liu, Y. Zhang, L. Tang, X-ray photoelectron spectroscopic studies of $Ba_{0.5}Sr_{0.5}Co_{0.8}Fe_{0.2}O_{3-[\delta]}$ cathode for solid oxide fuel cells, International Journal of Hydrogen Energy 34 (2009) 435–439.
[42] N. Merino, B. Barbero, P. Eloy, L. Cadús, $La_{1-x}Ca_xCoO_3$ perovskite-type oxides: identification of the surface oxygen species by XPS, Applied Surface Science 253 (2006) 1489–1493.
[43] S. Petrovic, L. Karanovic, P. Stefanov, M. Zdujic, A. Terlecki-Baricevic, Catalytic combustion of methane over Pd containing perovskite type oxides, Applied Catalysis B: Environmental 58 (2005) 133–141.
[44] M. Sosulnikov, Y. Teterin, X-ray photoelectron studies of Ca, Sr and Ba and their oxides and carbonates, Journal of Electron Spectroscopy and Related Phenomena 59 (1992) 111–126.
[45] R. Vasquez, X-ray photoelectron spectroscopy study of Sr and Ba compounds, Journal of Electron Spectroscopy and Related Phenomena 56 (1991) 217–240.
[46] A. Yan, V. Maragou, A. Arico, M. Cheng, P. Tsiakaras, Investigation of a $Ba_{0.5}Sr_{0.5}Co_{0.8}Fe_{0.2}O_{3-[\delta]}$ based cathode SOFC. The effect of CO_2 on the chemical stability, Applied Catalysis B: Environmental 76 (2007) 320–327.
[47] V. Young, T. Otagawa, XPS studies on strontium compounds, Applications of Surface Science 20 (1985) 228–248.
[48] M. Ghaffari, M. Shannon, H. Hui, O.K. Tan, A. Irannejad, Preparation, surface state and band structure studies of $SrTi_{(1-x)}Fe_{(x)}O_{(3-delta)}$($x = 0–1$) perovskite-type nano structure by X-ray and ultraviolet photoelectron spectroscopy, Surface Science 606 (2012) 670–677.
[49] A.E. Bocquet, A. Fujimori, T. Mizokawa, T. Saitoh, H. Namatame, S. Suga, N. Kimizuka, Y. Takeda, M. Takano, Electronic structure of $SrFe^{4+}O_3$ and related Fe perovskite oxides, Physical Review B 45 (1992) 1561.
[50] R.J. Lad, V.E. Henrich, Structure of [alpha]-Fe_2O_3 single crystal surfaces following Ar^+ ion bombardment and annealing in O_2, Surface Science 193 (1988) 81–93.
[51] P. Mills, J. Sullivan, A study of the core level electrons in iron and its three oxides by means of X-ray photoelectron spectroscopy, Journal of Physics D: Applied Physics 16 (1983) 723.
[52] H. Yamashita, Y. Ichihashi, M. Takeuchi, S. Kishiguchi, M. Anpo, Characterization of metal ion-implanted titanium oxide photocatalysts operating under visible light irradiation, Journal of Synchrotron Radiation 6 (1999) 451–452.
[53] I. Bersuker, I.B. Bersuker, The Jahn–Teller Effect, Cambridge University Press, 2006.
[54] A. Millis, B.I. Shraiman, R. Mueller, Dynamic Jahn–Teller effect and colossal magnetoresistance in La_{1-x} Sr_x MnO_3, Physical Review Letters 77 (1996) 175.
[55] M. Abbate, F. De Groot, J. Fuggle, A. Fujimori, O. Strebel, F. Lopez, M. Domke, G. Kaindl, G. Sawatzky, M. Takano, Controlled-valence properties of La_{1-x} Sr_x FeO_3 and La_{1-x} Sr_x MnO_3 studied by soft-X-ray absorption spectroscopy, Physical Review B 46 (1992) 4511.
[56] O. Haas, F. Holzer, S. Müller, J. McBreen, X. Yang, X. Sun, M. Balasubramanian, X-ray absorption and diffraction studies of $La_{0.6}Ca_{0.4}CoO_3$ perovskite, a catalyst for bifunctional oxygen electrodes, Electrochimica Acta 47 (2002) 3211–3217.
[57] I.R. Shein, V.L. Kozhevnikov, A.L. Ivanovskii, The influence of oxygen vacancies on the electronic and magnetic properties of perovskite-like $SrFeO_{3-x}$, Journal of Physics and Chemistry of Solids 67 (2006) 1436–1439.
[58] K. Zhu, Y. Cao, X. Wang, L. Bai, J. Qiu, H. Ji, Hydrothermal synthesis of sodium niobate with controllable shape and structure, CrystEngComm 14 (2012) 411–416.
[59] V. Kriventsov, D. Kochubey, Z. Ismagilov, O. Podyacheva, A. Nemudry, EXAFS study of Nb doped $Sr(Co/Fe)$ O_{3-x} perovskites, Physica Scripta 2005 (2005) 740.
[60] Y. Joly, D. Cabaret, H. Renevier, C. Natoli, Electron population analysis by full-potential X-ray absorption simulations, Physical Review Letters 82 (1999) 2398–2401.
[61] R. Vedrinskii, V. Kraizman, A. Novakovich, P. Demekhin, S. Urazhdin, Pre-edge fine structure of the 3d atom K X-ray absorption spectra and quantitative atomic structure determinations for ferroelectric perovskite structure crystals, Journal of Physics: Condensed Matter 10 (1998) 9561.
[62] T. Yamamoto, T. Mizoguchi, I. Tanaka, Core-hole effect on dipolar and quadrupolar transitions of $SrTiO_3$ and $BaTiO_3$ at Ti K edge, Physical Review B 71 (2005) 245113.
[63] D. Cabaret, B. Couzinet, A. Flank, J. Itie, P. Lagarde, A. Polian, Ti K pre-edge in $SrTiO_3$ under pressure: experiments and full-potential first-principles calculations, X-Ray Absorption Fine Structure–XAFS 13 (882) (2007) 120–122.
[64] M. Vracar, A. Kuzmin, R. Merkle, J. Purans, E. Kotomin, J. Maier, O. Mathon, Jahn–Teller distortion around Fe^{4+} in $SrTi_{1-x}Fe_xO_{3-d}$ from X-ray absorption spectroscopy, X-ray diffraction, and vibrational spectroscopy, Physical Review: Section B Condensed Matter 76 (2007) 174107.
[65] M. Belli, A. Scafati, X-ray absorption near edge structures (XANES) in simple and complex Mn compounds, Solid State Communications 35 (1980) 355–361.
[66] F. Bridges, C.H. Booth, M. Anderson, G.H. Kwei, J.J. Neumeier, J. Snyder, J. Mitchell, J.S. Gardner, E. Brosha, Mn K-edge XANES studies of $La_{1-x}A_xMnO_3$ systems (A=Ca, Ba, Pb), Physical Review B 63 (2001) 214405.
[67] H. Wang, J. Lewis, Effects of dopant states on photoactivity in carbon-doped TiO_2, Journal of Physics: Condensed Matter 17 (2005) L209.
[68] J.J. Rehr, Ifeffit Discussion (2002).http://cars9.uchicago.edu/pipermail/ifeffit/2002-October/000155.html.
[69] J. Mosselmans, J. Corker, J. Evans, J. Gauntlett, J. Rummey, EXAFS studies of catalyst generation, Catalysis Today 9 (1991) 175–182.
[70] M. Gyu Kim, H. Sang Cho, C. Hyun Yo, Fe K-edge X-ray absorption (XANES/EXAFS) spectroscopic study of the nonstoichiometric $SrFe_{1-x}Sn_xO_{3-y}$ system, Journal of Physics and Chemistry of Solids 59 (1998) 1369–1381.
[71] O. Haas, U. Vogt, C. Soltmann, A. Braun, W. Yoon, X. Yang, T. Graule, The Fe K-edge X-ray absorption characteristics of $La_{1-x}Sr_xFeO_{3-[delta]}$ prepared by solid state reaction, Materials Research Bulletin 44 (2009) 1397–1404.
[72] K. Kemner, S. Kelly, K. Orlandini, A. Tsapin, M. Goldfeld, Y. Perfiliev, K. Nealson, XAS investigations of Fe (VI), Journal of Synchrotron Radiation 8 (2001) 949–951.
[73] H. Falcon, J. Barbero, J. Alonso, M. Martinez-Lope, J. Fierro, $SrFeO_3$ perovskite oxides: chemical features and performance for methane combustion, Chemistry of Materials 14 (2002) 2325–2333.
[74] Y. Kuwahara, T. Ohmichi, K. Mori, I. Katayama, H. Yamashita, XAFS study on TiO_2 photocatalyst loaded on zeolite synthesized from Steel Slag, X-Ray Absorption Fine Structure–XAFS 13 (882) (2007) 708–710.
[75] M. Shimada, S. Nishio, T. Shimizu, K. Mori, T. Ohmichi, I. Katayama, H. Yamashita, XAFS study on nano-sized metal catalyst prepared by a photo-assisted deposition using Ti-containing mesoporous silica thin film photocatalyst, X-Ray Absorption Fine Structure–XAFS 13 (882) (2007) 799–801.
[76] F. Vasiliu, L. Diamandescu, D. Macovei, C. Teodorescu, R. Nicula, EXAFS investigation of iron local environment in metal-doped titania photocatalysts prepared by hydrothermal and high-energy ball milling routes, Journal of Materials Science: Materials in Electronics 20 (2009) 211–215.
[77] J. Davidson, No Time to Waste: Poverty and the Global Environment/Joan Davidson and Dorothy Myers with Manab Chakraborty, Oxfam, Oxford, 1992.